# Structure-Property Relationships of Differently Heat-Treated Binder Jet Printed Co-Cr-Mo Biomaterial

Meisam Khademitab <sup>a,1</sup>, Pierangeli Rodriguez de Vecchis <sup>b,1</sup>, Paulina Staszel <sup>a</sup>, Marcella K. Vaicik <sup>c</sup>, Markus Chmielus <sup>b,\*</sup>, Amir Mostafaei <sup>a,\*</sup>

- <sup>a</sup> Department of Mechanical, Materials, and Aerospace Engineering, Illinois Institute of Technology, 10 W 32<sup>nd</sup> Street, Chicago, IL 60616, USA
- <sup>b</sup> Department of Mechanical Engineering and Materials Science, University of Pittsburgh, Pittsburgh, PA 15261, USA
- <sup>c</sup> Department of Biomedical Engineering, Illinois Institute of Technology, 3255 South Dearborn Street, Chicago, IL, 60616 USA
- \* Corresponding authors

Email addresses: <a href="mailto:chmielus@pitt.edu">chmielus@pitt.edu</a> (M. Chmielus), <a href="mailto:mostafaei@iit.edu">mostafaei@iit.edu</a> (A. Mostafaei)

#### **Abstract**

This investigation systematically examines the influence of sintering temperature and aging treatment on the density, microstructure evolution, phase formation, and mechanical properties of a binder jet printed Co-Cr-Mo biomedical alloy. Sintering at 1380 °C for 2 h yielded a near-fully dense part (99.1%) with favorable mechanical properties (up to 325 HV<sub>0.1</sub> hardness and up to 693 MPa ultimate tensile strength). The grain size remained unchanged after aging at 800 °C for 24 h (89 $\pm$ 21 µm). Aging resulted in increased microhardness and tensile strength due to phase formation (Cr<sub>23</sub>C<sub>6</sub>, CrMo, and  $\epsilon$  phase), but a significant decrease in ductility. Consequently, the sintered and aged specimen exhibited higher hardness (522 HV<sub>0.1</sub>), yield strength (641 MPa), and ultimate tensile strength (854 MPa) compared to cast Co-Cr-Mo alloy. Biocompatibility testing with fibroblasts showed a cell viability of 95 $\pm$ 2%, indicating that binder jet printing did not affect the biocompatibility of the Co-Cr-Mo alloy. Exemplary printed parts including hip-joint, partial denture, and small-scale knee joint were successfully demonstrated. This study highlights the comparable properties of binder jet Co-Cr-Mo alloy to the cast alloy, affirming its potential for biomedical applications.

**Keywords:** Additive manufacturing; Sintering; Aging treatment; Phase formation; Dental material; Biocompatibility.

#### 1. Introduction

Co-Cr-based alloys (trademarked by Kennametal as Stellite<sup>®</sup>) are superalloys consisting of a Co matrix, hardened by high Cr content ( $\sim$ 30 wt. %). Cr provides both hardening, through the formation of carbides, and corrosion resistance, through the formation of a spontaneous  $Cr_2O_3$  passive oxide film. A third major element, such as W or Mo, is added in accordance with specific

<sup>&</sup>lt;sup>1</sup> These authors contributed equally to this work.

applications. Co-Cr-Mo alloys are used in a variety of applications including aerospace, gas turbines and dental and orthopedic implants [1–3], due to their combination of high hardness, strength, wear and corrosion resistance, and biocompatibility. The properties of this material are controlled by its chemical composition as well as the manufacturing and heat treatment processes. In general, the Co matrix has a hexagonal close packed (hcp,  $\varepsilon$ ) structure at room temperature, and a face centered cubic (fcc,  $\gamma$ ) structure at higher temperatures (above ~700 °C). However, due to the sluggish nature of the martensitic transformation, the high temperature fcc is usually retained at room temperature as a metastable matrix. This phase transition acts as a strengthening mechanism during plastic deformation as the hcp phase undergoes a strain-induced transformation to fcc [4–6]. Other than the matrix, the formation of secondary phases such as the brittle, intermetallic Co(Cr, Mo)  $\sigma$  phase and carbides play an important role in the properties of Co-Cr-Mo parts. The  $\sigma$  phase contributes to decreased ductility, fatigue and corrosion resistance [7], as it removes Cr out of solution and causes localized weak corrosion spots, also impacting biocompatibility [8]. However, the interaction of this phase with C results in the formation of intragranular M<sub>23</sub>C<sub>6</sub>, which can help increase hardness and strength when finely distributed [9].

To control the phases present, the manufacturing process and post-heat treatments must be carefully considered. Traditionally, Co-Cr-Mo parts have been manufactured through casting (ASTM F75 [10]), which is characterized by a dendritic microstructure, with heterogenous distribution of phases and precipitates that result in strength values of ~680 MPa [7]. More refined microstructures have been achieved through hot forging (above γ-stable temperatures) that resulted in higher strength (1450 MPa), but reduced ductility (2.5 %) [11,12]. However, since machining of these alloys is extremely difficult [13], powder-based techniques have been attempted to produce Co-Cr-Mo components. Metal injection molding (MIM) followed by sintering, allows to fabricate near net-shaped parts with homogenous grain microstructures. [14] reported grain sizes of 75 and 195 μm for sintering at 1300 °C and 1350 °C, respectively, with an as-sintered strength of 695 MPa and 10 % elongation. Furthermore, heat treatments contribute to tailor properties by dissolving detrimental phases or precipitating fine carbides. [14] reported a tensile strength of 763 MPa and 18 % elongation for MIMed pats after solution annealing at 1220 °C for 4 h, and a tensile strength of 962 MPa and 2 % elongation after aging at 750 °C for 20 h.

However, Co-Cr-Mo parts for biomedical applications require more intricate geometries for patient-matched and porous implants. Scaffold implants with internal and external microchannels promote cell and bone in-growth that help fix the implant in position (osseointegration). For biomedical implant, porosity is needed for better osseointegration, reduced elastic modulus, and production of lightweight biostructures. Through porosity (25-90 %, 200-1500 µm in size [15]), the overall metallic implant has a reduced elastic modulus that more closely resembles that of bone (to avoid stress shielding). As MIM is not able to produce internal channels, additive manufacturing (AM) has emerged as a potential solution for implant fabrication [16]. Laser-based AM techniques such as direct energy deposition (DED) and laser powder bed fusion (L-PBF) have yielded better results than traditional methods. DED, specifically laser engineering net shaping (LENS), has been used for cladding [17,18] and part fabrication [19]. Crack-free, high-density parts with high wear and corrosion resistance have been achieved through parameter optimization [19,20]. España et al. [21] reported LENS-printed parts that exhibited cell viability in partially porous, load-bearing implants designed with decreased elastic modulus (33-43 GPa), closer to that of bone (3-20 GPa). LPBF-printed and heat treated Co-Cr-Mo parts have also shown high density [22], improved distribution of carbides, complete dissolution of  $\sigma$  phase, smaller grain size (22-55) um [23]), and higher strength (979 MPa) [24]. Additionally, LPBF Co-Cr-Mo parts have been tested for corrosion and metal release susceptibility [25], and bone in-growth and implant fixation, proving them particularly efficient, especially when coated with Hydroxyapatite [26].

One limitation of fusion-based AM methods is the significant residual stress present in the resulting part, which can lead to the formation of cracks [15–18]. Binder jetting, an AM technique not reliant on a laser or electron beam, involves depositing powdered material layer by layer and selectively bonding it with a binder before consolidating it through sintering [32–36]. The use of binder jetting for metal fabrication shows great potential in the realm of AM due to its advantages, including rapid and cost-effective manufacturing, the production of stress-free, mechanically sound structures with intricate internal and external designs (as demonstrated in this study involving a complex denture framework with fine details, hip-joint and a small-scale knee model), and the achievement of isotropic properties in the final components [37,38]. Additionally, by leveraging conventional powder metallurgy techniques, binder jet printers can generate prototypes for biomedical applications using powdered materials [39–45], resulting in material properties and surface finishes comparable to those achieved through methods like powder injection molding (PIM) or traditional powder metallurgy [46].

Binder jetting offers several advantages over other AM technologies [47]. Firstly, it is highly versatile, compatible with a wide range of powdered materials, potentially surpassing powder bed fusion in material selection. Secondly, the process occurs at room temperature and atmosphere, avoiding issues like oxidation, residual stress, and the need for sealed chambers, resulting in a larger build volume. Thirdly, unlike fusion-based AM, binder jetting requires minimal support material and does not produce thermally induced stresses, making it suitable for complex geometries and overhanging features. Additionally, binder jetting possesses high production rates, cost-effectiveness, and suitability for specific geometries, making it a promising choice for various industries. Lastly, binder jetting offers the advantage over laser-based AM techniques of controlling porosity both through the CAD model and partial sintering [37,47,48], which is particularly interesting for biomedical implants. Binder jet printing has also been used to print Co-Cr-based parts [49,50], with inherited knowledge from MIM sintering. Although results are encouraging, research on binder jetting of Co-Cr-Mo has focused on optimizing printing parameters [51]. The influence of different sintering and heat treatments is not yet fully understood. Previous research from biocompatible and biodegradable alloys manufactured with this technology have shown good corrosion resistance, cytocompatibility and interconnected porosity [40,52].

Therefore, this project aimed to elucidate the effect of sintering temperature on the density, microstructure and mechanical properties of binder jetted and sintered Co-Cr-Mo parts, as well as the effect of aging treatments, especially with regards to carbide segregation. Mechanical properties were assessed through micro hardness and tensile test measurements. Mechanical properties improved with sintering temperature as porosity is removed, and further improved after longer periods of aging. Biomedical applications were also explored by binder jetting of complex shapes such as a small-scale hip and knee models as well as a dental framework. To assess biocompatibility, surface roughness was measured, and a cytotoxicity test was performed to confirm cell viability.

#### 2. Materials and methods

#### 2.1. Feedstock

Carpenter Technology Corporation provided gas atomized Co-Cr-Mo powder for this study. The morphology and elemental composition of the powder were examined using a scanning electron microscope (SEM, JEOL JSM 6510) equipped with energy dispersive X-ray spectroscopy (EDS). X-ray diffractometry (XRD, Bruker AXS D8 Discover) was employed for phase identification, utilizing Cu–K $\alpha$  radiation ( $\lambda$  = 1.54 Å, 40 kV, 40 mA), with a step size of 0.02° and a scan speed of 0.5 s/step. The XRD scans were conducted at room temperature, covering 2 $\theta$  scans from 20° to 95°. To prevent agglomeration, 1 g of the powder was suspended in isopropyl alcohol, and the particle size distribution (PSD) was analyzed using a Microtrac S3500 tri laser diffraction particle analyzer with spherical particle algorithms.

# 2.2. Manufacturing process

In order to investigate the relationship between structure and properties, cylindrical coupons (7 mm in height, 7 mm in diameter) were fabricated using an ExOne X1-Lab binder jet printer. The ExOne Company (now part of Desktop Metal) provided a solvent-based binder for the process. Printing parameters included a binder saturation of 60%, layer thickness of 100 μm, spread speed of 15 mm/s, feed to build powder ratio of 2, drying power control setting of 80%, spreader rapid traverse speed of 25 mm/s, right/left spread rapid traverse border of 5 mm, and drying time of 40 s. For the fabrication of mechanical testing specimens and complex structures like hip joints, small-scale knee joints, and partial denture frameworks [53], an ExOne Innovent binder jet machine was utilized due to the size limitations of the X1-Lab build box. The printing parameters for these parts consisted of a binder saturation of 60%, layer thickness of 100 μm, recoat speed of 120 mm/s, oscillator speed of 2100 rpm, roller speed of 350 rpm, roller traverse speed of 15 mm/s, and drying time of 15 s.

The green parts produced through binder jetting underwent a curing process at 200 °C using a Carbolite oven (type PF30). Subsequently, the cured parts were sintered in a Lindberg tube furnace placed in an alumina powder bed under vacuum (vacuum level was ~10<sup>-5</sup> bar). The sintering process involved a specific heating profile, which included heating at a rate of 5 °C/min from room temperature to 1000 °C, followed by a rate of 2.5 °C/min to reach the maximum holding temperature (ranging between 1240 and 1380 °C with 20 °C intervals). The parts were held at this maximum temperature for 2 h before cooling. The cooling process involved a rate of 1 °C/min to 1250 °C, followed by a rate of 5 °C/min to 500 °C, and finally furnace cooling to room temperature. For each sintering temperature, three samples were prepared. To investigate the effects of postheat treatment on microstructure and properties, the sintering condition that resulted in the highest relative density (>99%) was chosen, and aging treatments were conducted at 800 °C for holding times of 1 and 24 h.

## 2.3. Characterization techniques

The determination of *relative density* and *shrinkage* was carried out using the Archimedes principle (three-mass concept [54]) in deionized water, using an OHAUS AX324 precision balance with a resolution of 0.1 mg. Dimension measurements were performed to assess the shrinkage. Additionally, the relative density was determined through image analysis of the cross-sections (*xz* plane) of the sintered parts using ImageJ software [55]. *Microstructural observations* were conducted on cross-sections parallel to the build direction (*xz* plane). Slices were prepared,

mounted, ground, and polished according to the procedures outlined in reference [56]. Optical micrographs were captured using a Keyence digital optical microscope (OM) equipped with a dark field Z20 lens and multi-diffused adapter, as well as a Nikon Optiphot differential interference contrast (DIC) microscope. For microstructural characterization, compositional analysis, and fractography, scanning electron microscopy (SEM) equipped with energy-dispersive spectroscopy (EDS) was employed. Phase analysis and crystallography parameters, such as *d*-spacing values and lattice parameters, were determined using X-ray diffraction (XRD) with the scan parameters mentioned in section 2.1. The relative phase fraction was determined by analyzing the intensity of the primary reflections [57].

The *mechanical properties* of the samples were evaluated through Vickers microhardness tests conducted on the cross-sections using a Leco LM 800 microhardness tester with a 100-gf load applied for 10 s. Ten indentations were made, and the average value was recorded. Furthermore, rate-controlled tensile tests were performed using an MTS 880 machine with a crosshead speed of 5 mm/min. The as-printed dog-bone samples obtained from Innovent prints had initial dimensions of 60 mm length, 7 mm width, 5 mm thickness, and a gage length of 26 mm. After sintering, the dimensions changed to 5.75 mm width, 3.9 mm thickness, and a gage length of 20 mm. At least two samples were tested in the tensile experiments.

Surface roughness profiles were obtained using a KLA-Tencor Alpha-Step IQ surface profiler on two selected samples that were sintered at temperatures of 1300 °C and 1380 °C. Measurements were performed using a 5  $\mu$ m radius tip with a stylus load of 16.5 mg, as well as a 0.1  $\mu$ m radius diamond tip with a minimum applicable stylus load of 1 mg. The profiling of sample surfaces was conducted at a contact speed of 3  $\mu$ m/s. Scans were taken at six different locations with a scan rate of 10  $\mu$ m/s, a resolution of 0.1  $\mu$ m, and a sampling rate of 100 Hz. This setup ensured accurate results with minimal frequency noise. To evaluate anisotropy and artifacts, scans were performed in two orientations. A Gaussian Filter with a cut-off filter of 0.8 mm was applied. The arithmetic mean roughness ( $R_a$ ) and root mean square roughness ( $R_q$ ) values were calculated based on the obtained results from the stylus profilometer, following the averaging method outlined in the ISO 21920-2021 international standard.

Cell viability test - To assess the biocompatibility of the binder jetted Co-Cr-Mo (part sintered at 1380 °C), in vitro cytotoxicity assays were conducted on 3T3 fibroblast cells (ATCC) [58]. The 3D printed samples were first sterilized by autoclaving and then immersed in DMEM (Dulbecco's Modified Eagle Medium) for 24 h at 37 °C. Subsequently, the fibroblast cells were seeded in a 24-well tissue culture-treated plate at a density of 5×10<sup>4</sup> cells/well [59]. To determine the effect of direct contact with samples on cell viability, three groups were tested: a control group cultured in complete growth medium (DMEM, 10% Fetal Bovine Serum (FBS), 1% Pen Strep, and 1% L-Glutamine), an experimental group exposed to a mixture of 1:1 ratio of Co-Cr-Moexposed leachate (DMEM and 10% FBS) to complete media, and a second experimental group cultured in the leachate alone [59]. The cells were then incubated at 37 °C and 5% CO<sub>2</sub> for 5 days, with regular media changes every 2-3 days, in accordance with ISO 10993-5:2009(E) standards. To evaluate the cells viability, a live/dead staining assay was conducted at day 5 using the LIVE/DEAD Viability/Cytotoxicity Kit for Mammalian Cells by ThermoFisher Scientific in accordance with the manufacturer's protocol [59,60]. The cells were imaged using a Nikon A1 HD25 confocal imaging system with Fully motorized Nikon Eclipse Ti2-E inverted microscope with epifluorescence. The obtained images were then processed on ImageJ to obtain percentage of viable cells which was quantified by estimating the area of cells in the well stained green (arealive)

and those stained red (area<sub>dead</sub>) using confocal microscopy. *Cell attachment test* – To conduct a direct contact cell attachment experiment on Co-Cr-Mo samples, first, 3T3 fibroblast cells were fluorescently stained with PKH26 Red Fluorescent Cell Linker Mini Kit for General Cell Membrane Labeling (Sigma-Aldrich), following the manufacturer's instructions [61]. After the cells were stained, a drop of the cell solution was placed on the surface of the 3D printed sample. The sample was then incubated for 24 h to allow for adequate cell attachment before being flipped face down into the well for imaging. The cells were imaged using a Nikon Eclipse Ti2 confocal microscope. The obtained images were then processed on ImageJ to obtain the average area of cell coverage on the sample. A summary of the procedures is demonstrated in Figure 1.

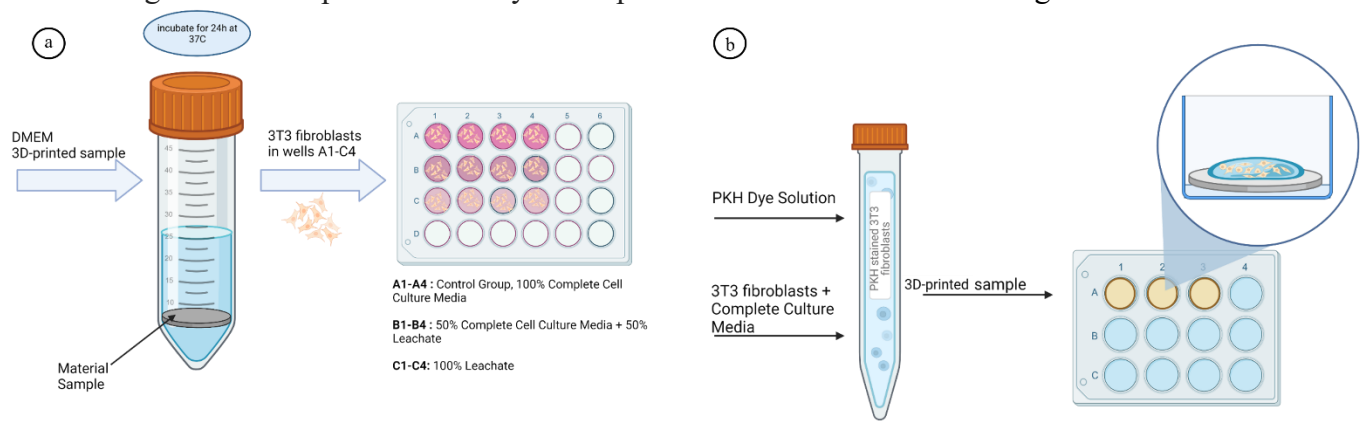


Figure 1. Schematics of procedures for (a) cell viability and (b) cell attachment tests.

# 3. Results and discussion

## 3.1. Powder feedstock characterizations

SEM micrographs in Figure 2a,b demonstrate size distribution and spherical morphology of the used powder with small satellites on their surface. Also, a dendritic structure was obvious on the particle surfaces which was associated with the rapidly solidified gas-atomized Co-Cr-Mo powder. The PSD analysis result is shown in Figure 2c in which  $d_{10}$ ,  $d_{50}$ , and  $d_{90}$  values were about 26  $\mu$ m, 33  $\mu$ m, and 40  $\mu$ m, respectively. The chemical composition of the nominal Co-Cr-Mo alloys (also known as Stellite 21) was compared with the manufacturer, and our measurement using EDS analysis are given in Table 1.

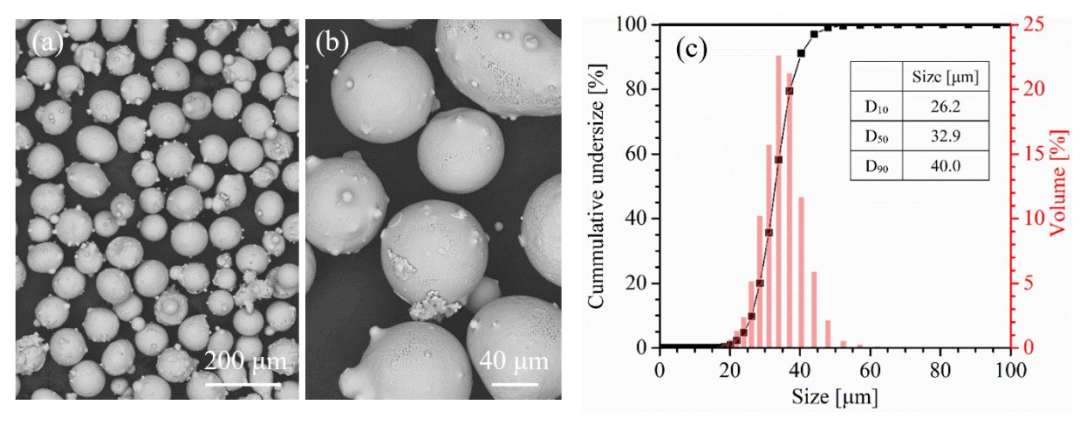


Figure 2. Co-Cr-Mo alloy powder (a,b) SEM micrographs and (b) PSD analysis.

Table 1. Chemical composition of the Co-Cr-Mo alloy in weight percent [wt.-%]. The EDS analysis on the powder is based on three EDS point analysis and reporting the average values.

	Co	Cr	Mo	С	N	Si	Mn	Fe	S	Ni
Nominal composition (ASTM F1537)	Bal.	26-30	5-7	<0.14	-	<1	<1	0.75	-	<1
Manufacturer analysis	Bal.	27.72	6.07	0.12	0.17	0.71	0.70	0.03	0.001	0.02
EDS powder analysis	Bal.	29.19	5.01	-	-	0.69	0.89	-	0.16	-

## 3.2. Density measurements

Relative density measurements were studied using Archimedes method and solid area fraction based on 2D image analysis of optical micrographs on sectioned specimens parallel to the build direction (see Figure 3.). Also, the dimension reduction and volume shrinkage were measured on samples and results were shown in Figure 3.b. Depending on the sintering temperature, linear shrinkage varied from 2% at 1240°C to 19% at 1380°C. This indicates that when creating complex parts via binder jet printing, it is essential to scale up their dimensions during the printing stage to ensure the final dimensions are met after sintering. The standard deviation of the average dimension reduction was less than 1%. The as-printed part after curing step (green part) had a relative density of ~50%. Onler et al. binder jet printed Co-Cr-Mo powder with  $D_{50} = 35 \mu m$  resulting in green parts with a relative density of 46% [51]. In our study, the relative density reached 53±2% and 64±2% in samples sintered at 1240 °C and 1320 °C, respectively. The minimal evolution in relative density and linear behavior in densification might be related to the rearrangement of pores and initial stage of densification, in which pores were expected to be interconnected. As the sintering temperature increased to 1340 °C, a sudden increase in density was observed. This suggests a transition from initial to intermediate stage sintering in which isolated pores evolve in the microstructure. By further increasing temperature to 1360 °C, a relative density of 89±2% was achieved. The highest relative density of ~99.8% was attained at sintering temperatures of 1380 °C. When higher sintering temperatures were applied (>1380 °C), surface melting occurred, and coupons lost their cylindrical shape. In an earlier work by Mostafaei et al. [50], Co-Cr-W powder with a PSD of 90-110 μm was binder jetted and sintered and a final relative density of 99.8% was also reported. In other works [5,62], such a high density was reported after hot isostatic pressing. Further microstructure analysis is elaborated in the following section.

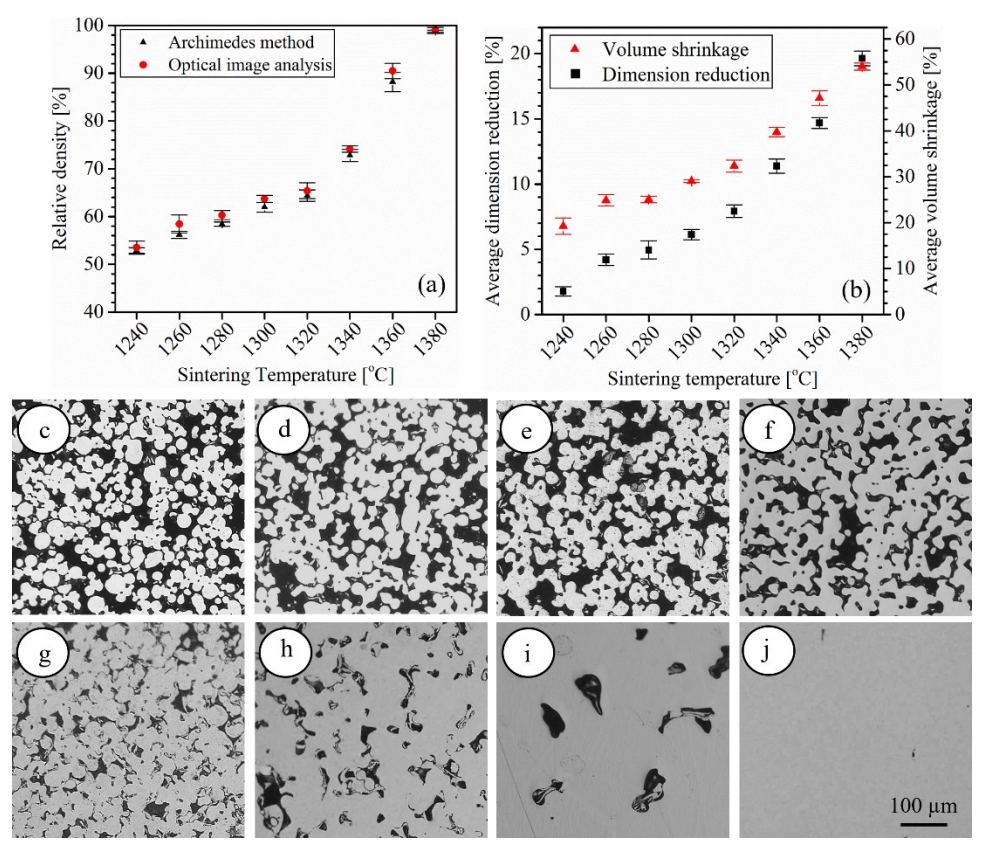


Figure 3. Measured (a) relative density and solid area fraction obtained from the Archimedes method and optical micrograph analysis using ImageJ, and (b) average dimension reduction and volume shrinkage on binder jetted Co-Cr-Mo followed by sintering at (c) 1240 °C, (d) 1260 °C, (e) 1280 °C, (f) 1300 °C, (g) 1320 °C, (h) °C, 1340 °C, (i) 1360 °C, and (j) 1380 °C.

#### 3.3. Phase analysis using XRD

To analyze phases in binder jetted Co-Cr-Mo alloy, XRD was carried out on differently sintered and aged samples and results are shown in Figure 4. Co-Cr-based alloys typically have  $\gamma$ -Co (fcc) and/or  $\varepsilon$ -Co (hcp) phases as well as carbides and intermetallic compounds in the microstructure, which can be affected by chemical composition, manufacturing process and cooling rate, and post heat treatment. The as-received Co-Cr-Mo powder showed γ-Co (fcc) single phase (formation of Co solid solution containing Cr and Mo in substitutional solid solution), which was associated with the rapid solidification of the liquid droplets during atomization. The calculated lattice parameter of the Co-Cr-Mo powder was a = 0.359 nm which is in agreement with those reported in literature [63,64]. When sintered between 1240-1340 °C, the Co matrix showed both y-Co ( $\sim$ 95%) and  $\varepsilon$ -Co ( $\sim$ 5%) phases. For instance, crystallographic parameters in the sample sintered at 1340 °C were calculated. The lattice parameter in  $\gamma$ -Co was a = 0.362 nm, indicating peak shift to smaller  $2\theta$  values. Also, the calculated lattice parameters in  $\varepsilon$ -Co were a=0.258 and c = 0.410 nm with a c/a ratio of 1.59. A higher  $\gamma$ -Co (fcc)  $\rightarrow \varepsilon$ -Co (hcp) phase transformation was observed after sintering at  $\geq 1360$  °C. The fraction of hcp phase increased to about 90% and 95% in samples sintered at 1360 °C and 1380 °C, respectively. For the highest density samples (sintered at 1380 °C), the lattice parameter of y-Co was a = 0.358 nm, indicating a peak shift to higher  $2\theta$  values compared to the lower sintering temperatures. The calculated lattice parameters in  $\varepsilon$ -Co were a=0.253 and c=0.411 nm with a c/a ratio of 1.62. Ziebowicz et al. [65] reported that powder injection molded Co-Cr-Mo showed < 10% of  $\gamma$ -Co after sintering while a laser powder bed fused part had up to  $\sim 86\%$   $\gamma$ -Co attributed to different cooling rates [66]. In all sintered samples, there were no clear diffraction peaks of other phases, especially carbides. After the aging treatment (800 °C for 24 h), few additional diffraction peaks were detected including Cr<sub>23</sub>C<sub>6</sub> and Cr-Mo phases. The calculated lattice parameters in  $\varepsilon$ -Co (aged sample for 24 h) were a=0.254 and c=0.409 nm with a c/a ratio of 1.61. As indicated in SEM-EDS analysis, both phases were present at the grain boundaries. No oxide diffraction peaks were seen because of sintering under vacuum condition in the presence of Ti sponges as strong O getters.

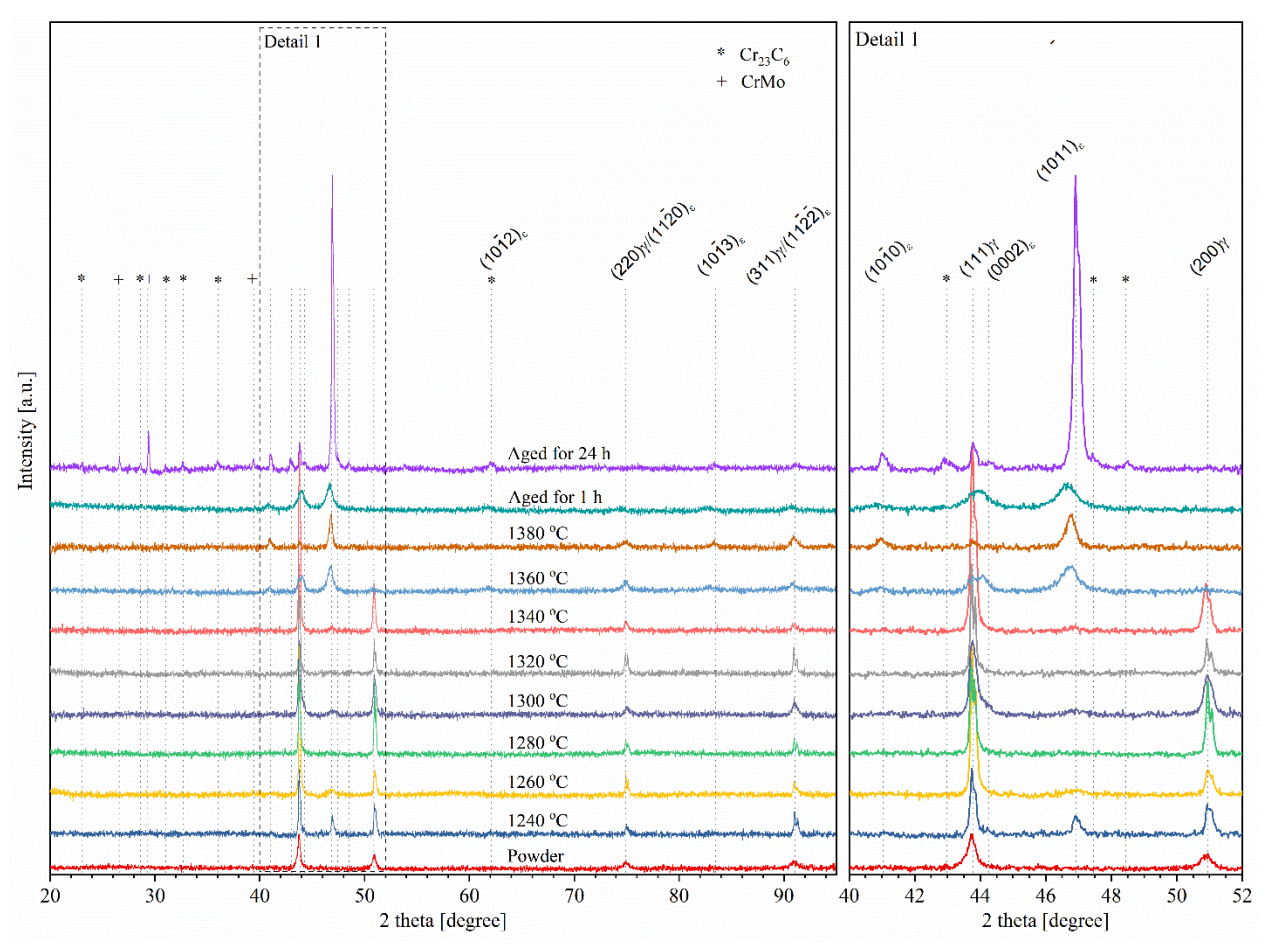


Figure 4. X-ray diffraction patterns of feedstock and binder jetted Co-Cr-Mo parts sintered and aged at different conditions. The reference XRD patterns of 04-016-6869 ( $\gamma$ -Co with fcc structure), 04-017-1160 ( $\varepsilon$ -Co with hcp structure), and 04-007-5437 (Cr<sub>23</sub>C<sub>6</sub>) were used for indexing main peaks.

## 3.4. Microstructure observations

The information gathered about the microstructural evolution of binder jetted Co-Cr-Mo alloy in the previous sections suggests the presence of three distinct sintering regimes for the used temperatures. From the XRD patterns (Figure 4) and SEM micrographs (Figure 5), a significant increase of  $\varepsilon$  (hcp) over  $\gamma$  (fcc) is observed as sintering temperature increases. This increase is also observed through twinning in DIC images (Figure 6) of the sintered part at 1380 °C. Additionally, the expected increase in density and evolution of grain morphology from the spherical, particle-

like grains at the lower temperatures to the larger equiaxed grains at the higher temperatures is also evident from SEM images. Lastly, the density (Figure 3) and grain evolution (Figure 5) show three separate incremental regions of solid volume fraction and grain size, respectively.

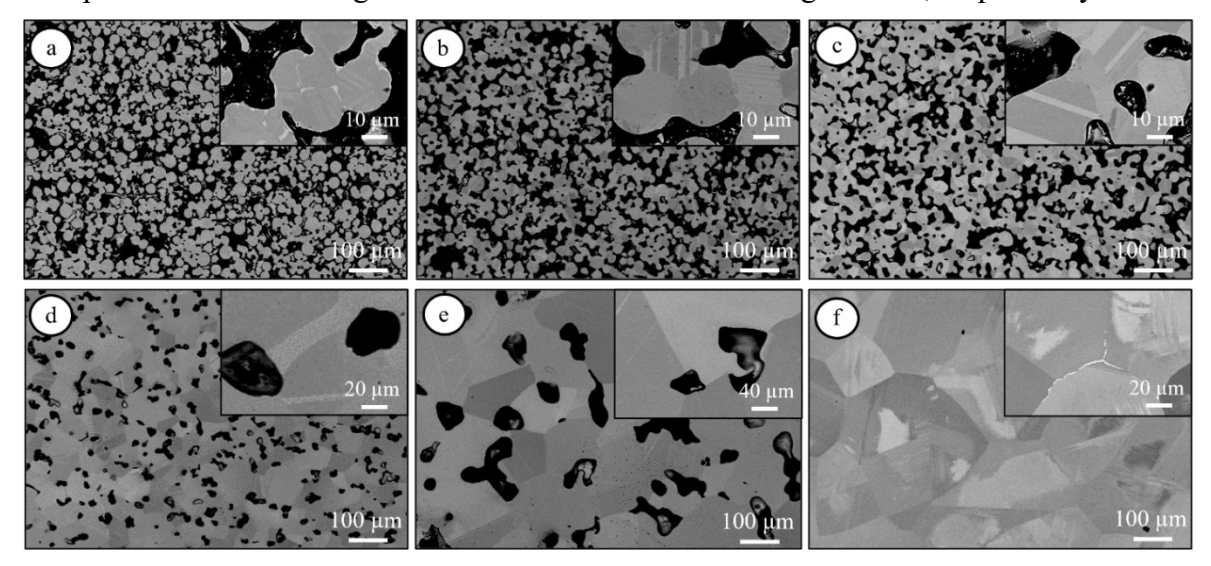


Figure 5. SEM micrographs on polished cross-sections of binder jetted Co-Cr-Mo parts sintered at (a) 1240 °C, (b) 1280 °C, (c) 1320 °C, (d) 1340 °C, (e) 1360 °C, (f) 1380 °C.

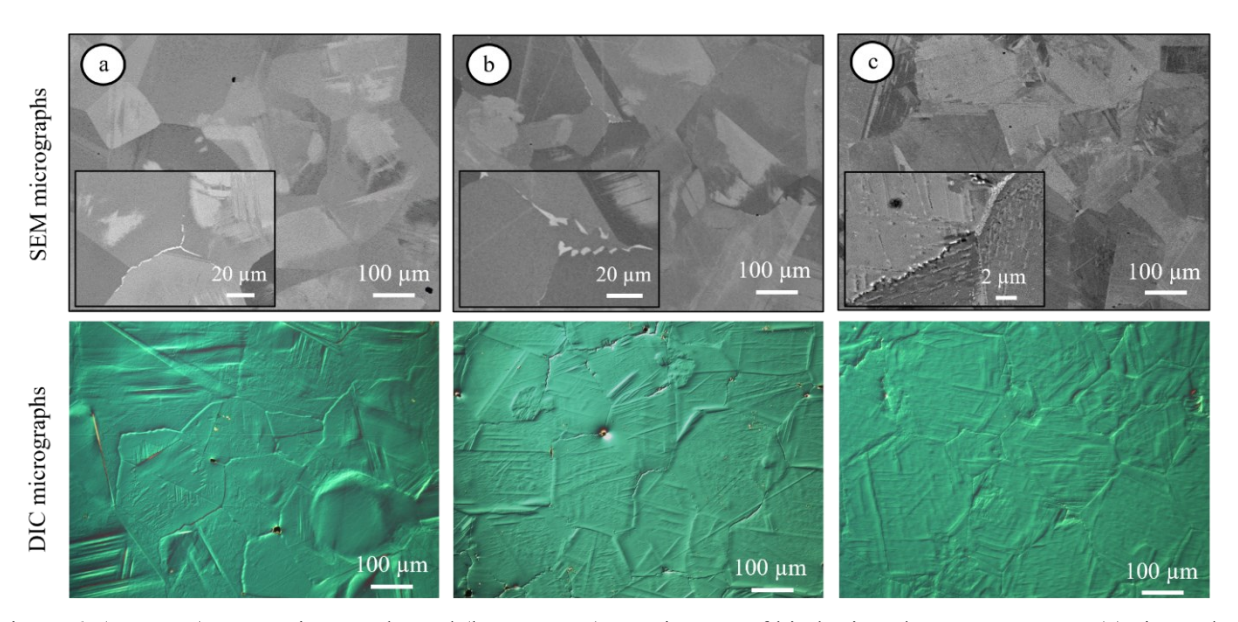


Figure 6. (Top row) SEM micrographs and (bottom row) DIC images of binder jetted Co-Cr-Mo parts (a) sintered at 1380 °C for 2 h, (b) aged at 800 °C for 1 h, and (c) aged at 800 °C for 24 h.

As density evolved from the green state, sintering at low temperatures, 1240-1260 °C, showed a small increment up to 59 %, while grain size remained constant at 17.5  $\pm$  0.8  $\mu$ m. As density slowly increased from 60 % to 64% for sintering temperatures between 1280 °C and 1320 °C, the grain size also remained nearly constant, changing between 20.4  $\pm$  0.8 and 20.8  $\pm$  1.1  $\mu$ m (these values are consistent with those reported by [67] for 2 h sintering of Co-28Cr-6Mo at 1200 °C, and by [68] for 1 h sintering at 1250 °C and 1300 °C). With a further increase in temperature

to 1340-1360 °C, a sudden and significant increase in density (75 - 89 %) is accompanied by a significant increase in grain size (49.7  $\pm$  11.2 to 122.5  $\pm$  11.2  $\mu$ m). And, at the highest sintering temperature, 1380 °C, full density was achieved along with further grain growth reaching 182.4  $\pm$  3.4  $\mu$ m. The three first regions appear to be the initial, intermediate, and final stages of solid-state sintering, respectively, followed by a last stage of super-solidus phase sintering for the highest temperature, as further elaborated in section 3.5.

The effect of the aging treatment on the microstructural evolution is shown in Figure 6 and Figure 7. After 24 h, aging at 800 °C had a significant effect on  $\gamma$ -Co (fcc)  $\rightarrow \varepsilon$ -Co (hcp) phase transformation and appearance of twinning in each grain and caused a small grain size increase to 192.8  $\pm$  6.2  $\mu$ m, as well as dissolution of the intergranular phase that appeared during sintering at 1380 °C. Further analysis of the phase evolution is discussed in the section below.

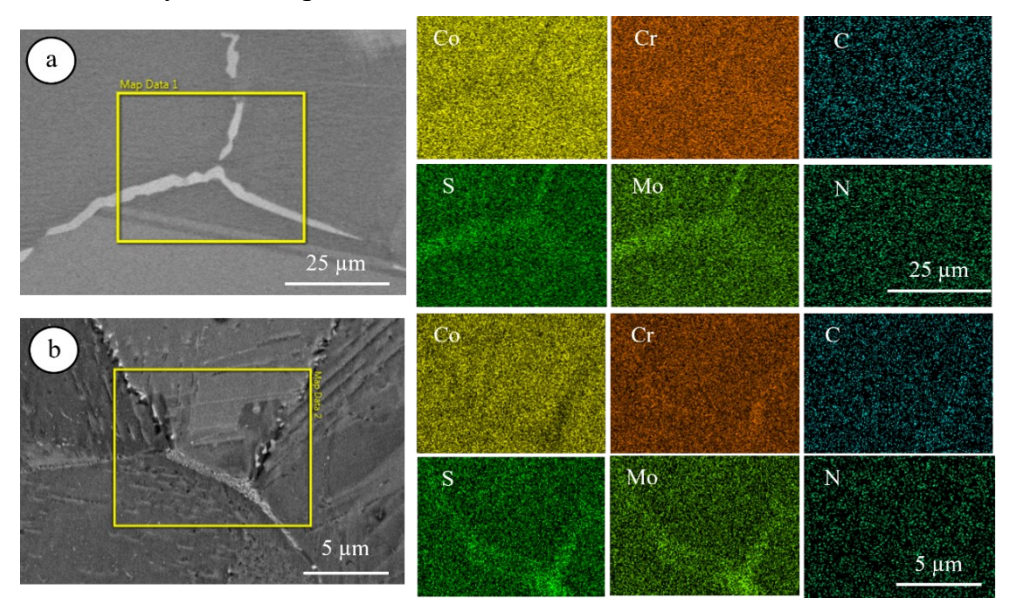


Figure 7. SEM-EDS of binder jetted Co-Cr-Mo parts (a) sintered at 1380 °C for 2 h and (b) aged at 800 °C for 24 h.

## 3.5. Microstructural evolution during sintering and heat-treatment of Co-Co-Mo alloy

Co-Cr-Mo alloy has been reported to have a solidus temperature close to 1363 °C and liquidus near 1419 °C [69,70]. The *initial* or *low temperature sintering regime* occurs from 1240 °C to 1260 °C, where densification happens slowly with respect to temperature. These microstructures are characterized by large, interconnected porosity networks with particle-like grains necked together. Particle necks and their periphery are surrounded by a clear phase (Figure 5), rich in Mo and Cr, presumably a continuous M<sub>23</sub>C<sub>6</sub> carbide, stable at these temperatures [71]. Additionally, as shown in Figure 8, grain growth is stagnant at this stage (similar to early sintering of injection molded SS 316 [72]). Twinning is observed in some grains, suggesting the presence of hcp phase, in an otherwise dominant fcc matrix. The *intermediate temperature sintering regime* occurs from 1280 °C to 1320 °C, characterized by a progressive increase in density but still no significant change in grain size, although the necked particles are now more coalesced. During this stage, the pore networks are broken up into smaller sections and some round individual pores. The dominant phase also changes, with now an hcp matrix, little fcc phase present, and no continuous carbides. However, at the grain boundaries, nano-sized Cr, Mo-rich carbides are observed

(possible remaining from incomplete M<sub>23</sub>C<sub>6</sub> dissolution or transformation into M<sub>6</sub>C before completely dissolving in the matrix [73,74]). The *final stage of sintering* occurs from 1340 °C to 1360 °C, where densification reaches 90 %. There is a sudden and significant increase in grain size, common of this stage, as density increases beyond 70 % [75], with smaller, rounder pores at grain boundaries and triple points. Additionally, no carbides were observed at grains or grain boundaries, which appeared as straight, clear edges. The hcp content also increased as indicated by XRD results. Lastly, for the highest temperature (1380 °C), *supersolidus liquid phase sintering* is likely to have taken place, as the sintering temperature is above the solidus temperature reported by [69], which led to complete pore filling, full densification, and a final grain size increase. The liquid phase is evidenced by the segregation of a continuous Cr-rich phase along grain boundaries, similar to that found by [69] when sintering at 1325 °C (although they reported excess C as a result of the used binder that resulted in incipient melting even at that temperature). A summary of the sintering regimes evolution is shown in Figure 8.

Aging at 800 °C had a significant effect after 24 h. An increase in hcp phase occurred, consistent with the Time-Temperature-Transformation diagrams designed by [76,77] for these aging conditions. Furthermore, a considerable amount of sub-micron Cr and Mo-rich carbides were present along grain boundaries, similar to those found for intermediate stage sintering and in previous studies [78,79]. Additionally, the continuous Cr-rich segregation produced during liquid phase sintering was broken up into smaller sections after 1 h aging and disappeared after 24 h. However, a pearlitic Cr-rich phase appeared at some grain boundaries. This structure has been previously identified as lamellar M<sub>23</sub>C<sub>6</sub> carbides, observed at interdendritic regions of as-cast Co-Cr-Mo after heat treating at 1000 °C [80], and lamellar intergrowth of M<sub>23</sub>C<sub>6</sub> and M<sub>7</sub>C carbides, rich in Mo and Cr respectively [81]. However, the sole presence of M<sub>23</sub>C<sub>6</sub> is more likely, as confirmed by XRD, and as found in wrought and as-cast Co-Cr-Mo alloys [82,83], as well as in MIMed and aged (750 °C for 20 h) samples [14].

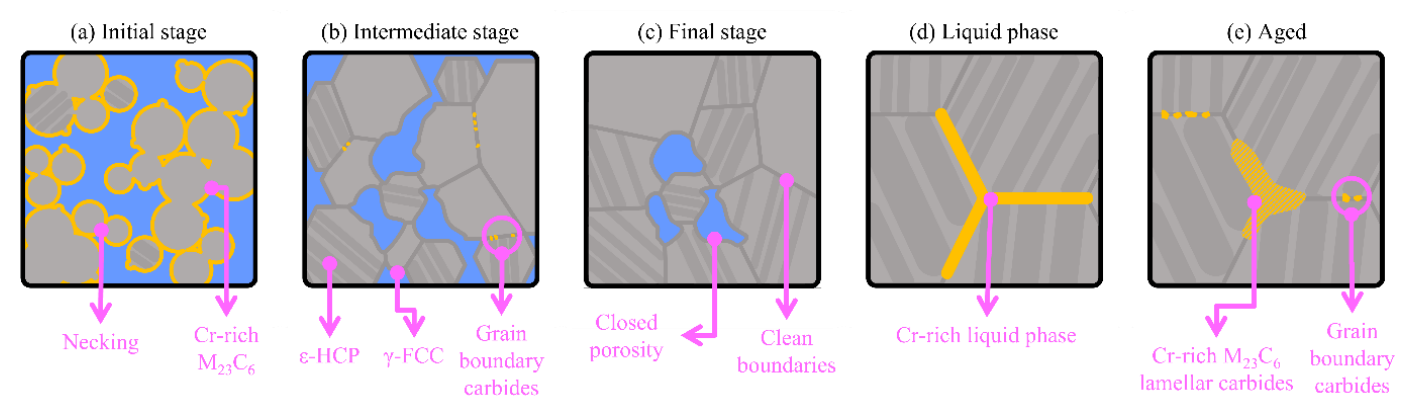


Figure 8. Schematic of the microstructural evolution of binder jetted Co-Cr-Mo alloy during consolidation, showing (a-c) the three stages of solid-state sintering, (d) liquid phase sintering and (e) the aged condition.

## 3.6. Mechanical properties and fractography

*Microhardness* – The influence of sintering temperature and aging treatment microhardness are summarized in Figure 9a. It is shown that when the sintering temperature was 1240 °C, the

average hardness value was 93 HV<sub>0.1</sub> and it gradually increased to 293 HV<sub>0.1</sub> with increasing sintering temperature to 1380 °C. This is a typical trend in powder metallurgy in which the density increases with increasing sintering temperature due to pore elimination (considering minimal grain growth or elemental segregation at grain boundaries) [36,50,84,85]. An aging treatment at 800 °C for 24 h on the highest relative density specimens (sintered at 1380 °C) further improved microhardness to 522 HV<sub>0.1</sub> which could be associated with the formation of nano-scale carbides within grains and  $\gamma$ -Co (fcc)  $\rightarrow \varepsilon$ -Co (hcp) phase transformation [50]. The reported microhardness value for cast alloy Co-Cr-Mo is ~300 HV and can reach ~550 HV after aging treatment [86].

Tensile test – Strength and ductility of the fully densified Co-Cr-Mo specimens as well as post heat treated samples at 800 °C are shown in Figure 9b and values summarized in Table 2. The sintered sample at 1380 °C (led to a near full dense part) showed an ultimate yield strength of ~325 MPa, ultimate tensile strength (UTS) of ~686 MPa, and elongation of ~29%. However, aging altered these values to ~420 MPa, ~750 MPa, and 14% (aged at 800 °C for 1 h) or ~542 MPa, ~854 MPa, and 3% (aged at 800 °C for 24 h), respectively. Also, the calculated elastic modulus was in the order of 50-60 GPa. The enhanced yield strength and UTS as well as reduction in ductility after aging was associated with y-Co (fcc)  $\rightarrow \varepsilon$ -Co (hcp) phase transformation and carbide formation at the grain boundaries. The yield strength, UTS, and elongation of the cast Co-Cr-Mo alloy were reported as 450 MPa, 655 MPa, and 8%, respectively [87]. Thus, different heat treatment of binder jet printed Co-Cr-Mo can provide desirable mechanical properties based on applications. This is in agreement with Kilner et al. [83], who showed that the mechanical properties of Co-Cr alloys relied on the heat treatment condition and carbon content (highest ductility was reported for an alloy with C content as low as 0.07 wt.%). Furthermore, porous samples sintered at 1300 °C with a relative density of ~64% were subjected to testing. The results revealed a reduction in all mechanical properties attributed to the presence of remaining pores. Nevertheless, it is noteworthy that the elastic modulus of the porous sample was < 20 GPa, suggesting the potential for achieving lower values that could find favorable applications as implants, such as creating gradient structures with varying porosity levels [88].

Fractography – Topology of fracture surfaces were studied using optical and SEM and results are shown in Figure 9c-d. No pore was observed on the SEM micrographs indicating an effective sintering procedure on mechanical testing samples resulting in near fully dense parts. The SEM micrographs taken from fractured surfaces of the sintered specimen showed mostly brittle fractures with minimal ductile fracture features (i.e., dimples). Also, equiaxed grains were obvious, indicating intergranular fracture, and only a few micro-cracks were detected at the grain boundaries. After aging treatment, the fraction of  $\varepsilon$  phase was significantly increased which resulted in partially transgranular fracture with no dimples present. Wedge-type cracks were seen on the fracture surface of aged sample for 24 h, which was associated with the quasi-cleavage fracture and typically occurred along faceted {111} planes [89–91].

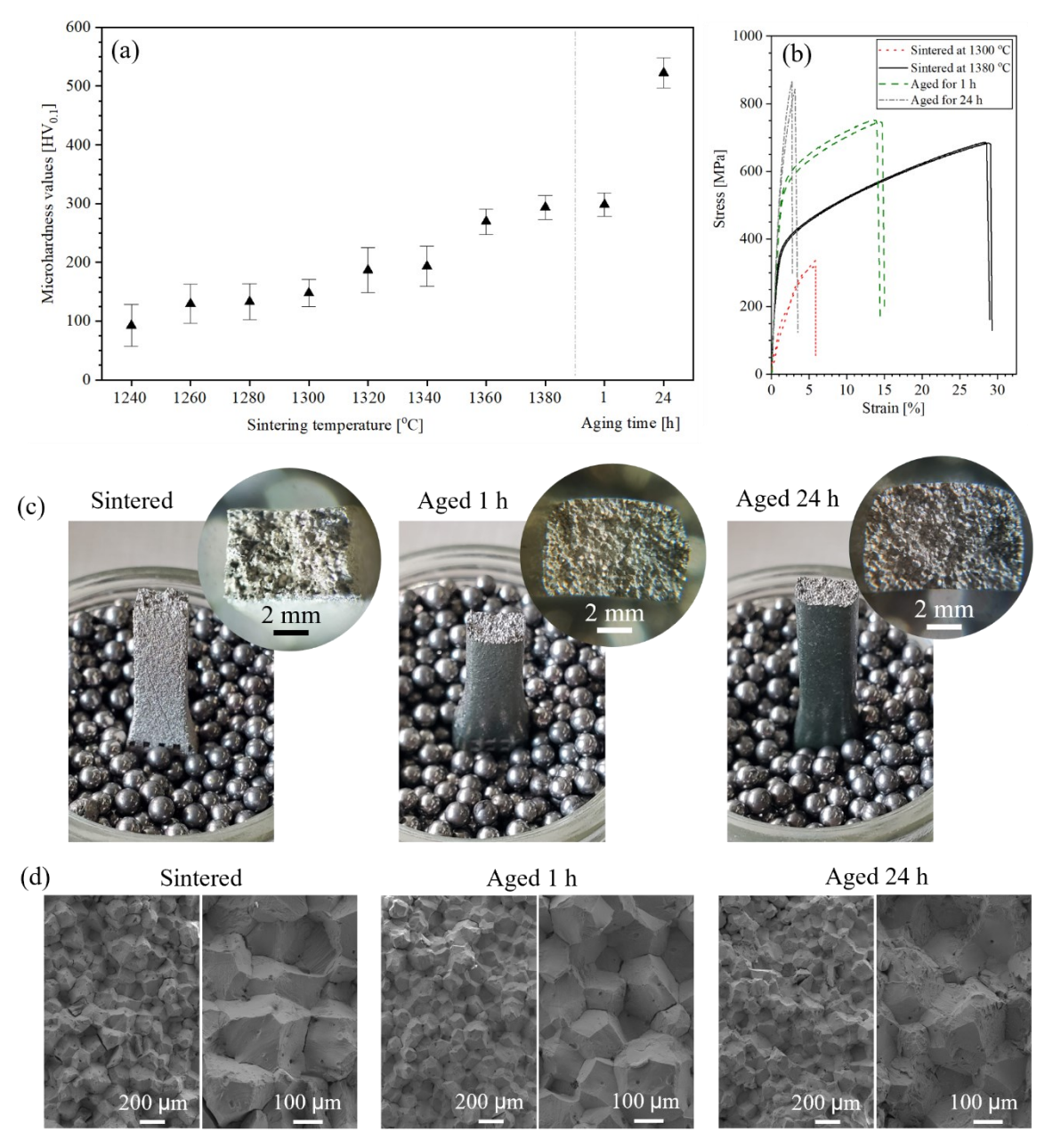


Figure 9. (a) Microhardness values and (b) stress-strain curves from the differently heat-treated binder jetted Co-Cr-Mo parts. Micrographs from the fracture surface of binder jetted Co-Cr-Mo parts after tensile tests sintered at 1380 °C for 2 h and aged at 800 °C for 1 h or 24 h: (c) optical and (d) SEM micrographs.

Table 2. Average values of UTS, YS<sub>0.2%</sub> and elongation of the differently heat-treated binder jetted Co-Cr-Mo parts.

S1	Yield stress	UTS	Elongation	Microhardness	
Samples	[MPa]	[MPa]	[%]	$[HV_{0.1}]$	
Sintered at 1300 °C for 2 h	$278 \pm 6$	$323 \pm 12$	$5.8 \pm 0.2$	$151 \pm 33$	
Sintered at 1380 °C for 2 h	$325 \pm 11$	$686 \pm 2$	$28.8 \pm 0.3$	$293 \pm 37$	
Aged at 800 °C for 1 h	$420 \pm 7$	$750 \pm 3$	$14.4 \pm 0.4$	$298 \pm 20$	
Aged at 800 °C for 24 h	$542 \pm 14$	$854 \pm 12$	$3.0 \pm 0.2$	$522 \pm 26$	
Cast alloy Co-Cr-Mo (ASTM F75-23)	450	655	8	300	

# 3.7. Surface roughness

The study also aimed to analyze the surface roughness of binder jetted parts after sintering, which is important for porous biomaterials used as implants in the human body. Two sintering temperatures were selected, and surface roughness was measured to compare surface topology. Calculated roughness values revealed an  $R_a = 3.19 \pm 0.08~\mu m$  and  $R_q = 3.78 \pm 0.20~\mu m$  in the sintered part at 1300°C, whereas values decreased to  $R_a = 0.53 \pm 0.03~\mu m$  and  $R_q = 0.70 \pm 0.06~\mu m$  in the sintered part at 1380 °C. Qualitative results from cross sectional micrographs showed a rough surface at 1300 °C, while the surface was smoothed at the maximum sintering temperature of 1380 °C (see Figure 10a-b). In contrast, another study [92] using binder jetted 625 alloy with feedstock of PSD 15-53  $\mu$ m showed roughness values of  $R_a = 7.65 \pm 1.58~\mu m$  and  $R_q = 12.01 \pm 2.52~\mu m$  in the as-sintered condition with a relative density of 99.2%.

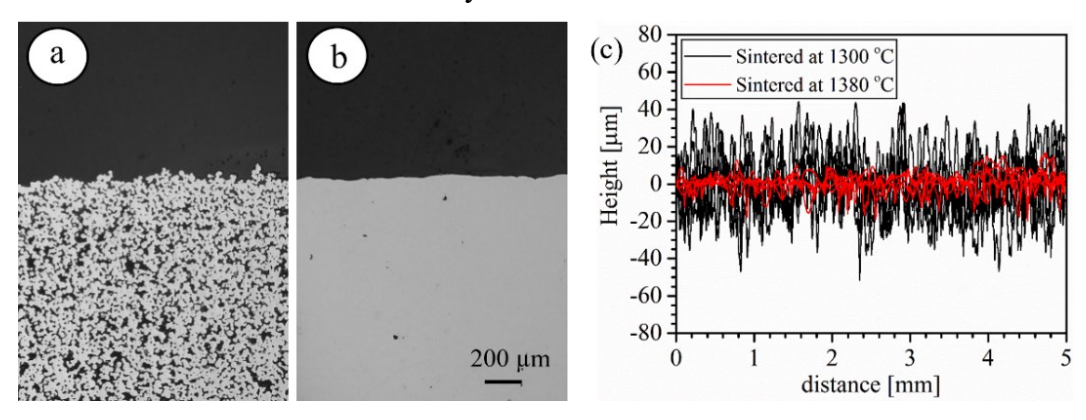


Figure 10. Optical micrographs at the cross-section of binder jetted Co-Cr-Mo parts sintered at (a) 1300 °C and (b) 1380 °C in which porosity and surface features were evaluated. (c) Line scans of topography results collected by stylus profilometry.

# 3.8. Biomedical application and cytotoxicity study

The research showcased the production of complex biomedical parts using binder jetting followed by sintering. Examples such as the hip-joint, partial denture frame, and small-scale knee joint highlighted the ability of binder jetting to create intricately designed parts. Sintering played a crucial role in consolidating the printed parts and maintaining their original shape. Controlling the densification rate and shrinkage during sintering was essential to prevent deformation and sagging of complex structures. The use of an alumina powder bed ensured uniform heat conduction and prevented structural deformations. The selection of sintering and aging treatments depended on the desired porosity and mechanical strength of the parts. The results demonstrated that binder jetting is capable of producing complex, high-density parts suitable for biomedical applications. The findings of the study provide valuable insights into the design of sintering and aging treatments to achieve the desired microstructure and properties of the final parts.

Cell viability test - Figure 12 provides data on the average percentages of live and dead cells in three groups after they have been in contact to the binder jetted and sintered Co-Cr-Mo alloy for 5 days. The first group (Control) has an average of 97±1% live cells, indicating a high level of consistency within the group. The second group (Experimental Group A) had an average of 95±2% live cells, suggesting a greater variation in cell viability within this group. Similarly, the third group (Experimental Group B) had an average of 95±2% live cells. These percentages

suggest that the majority of cells in each group were alive, with the first group having the highest percentage of live cells. The percentage of dead cells is relatively low in all three groups, indicating that the conditions for cell growth and survival were generally favorable. This means that the elemental leachate did not have a significant effect on the viability and confluency of the 3T3 fibroblast cells, which is the desired outcome. *Cell attachment test* - The red fluorescence is an indicator that the 3T3 fibroblasts have successfully attached to the Co-Cr-Mo sample, which is the desired outcome in this cell attachment experiment (see Figure 12). The images were processed on ImageJ and the percent of area occupied by the cells was determined. The graph contains the number of cells attached on 2 different samples with identical properties. The average area of cells attached to the samples was  $8\pm2\%$  after 24 h of contact with the sample.

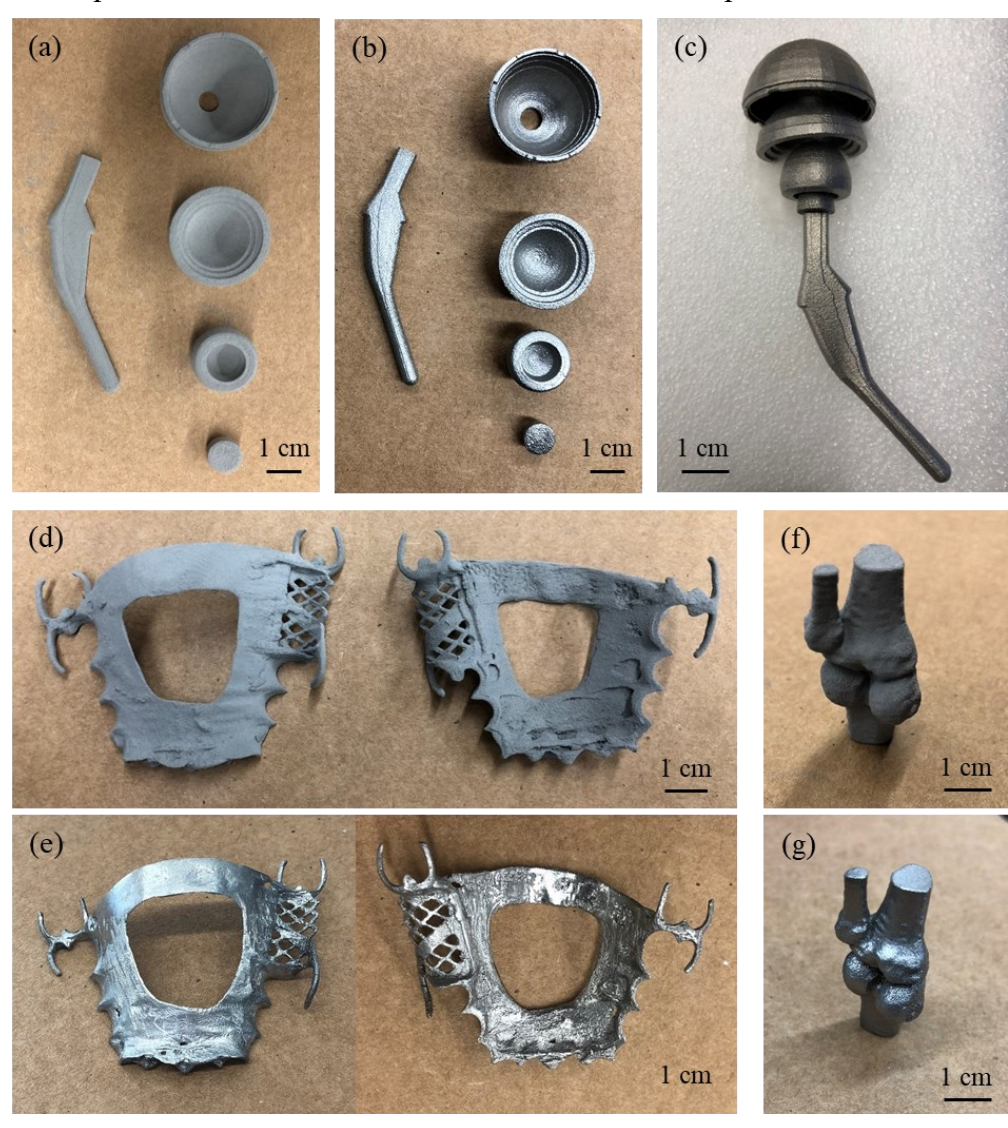


Figure 11. Exemplary photographs of prototype parts manufactured by binder jetting and sintering of Co-Cr-Mo powder. (a,d,f) green parts and (b,c,e,g) sintered samples at 1380 °C for 2 h. (a-c) hip joint, (d,e) partial denture frame work; and (f,g) small-scale knee joint.

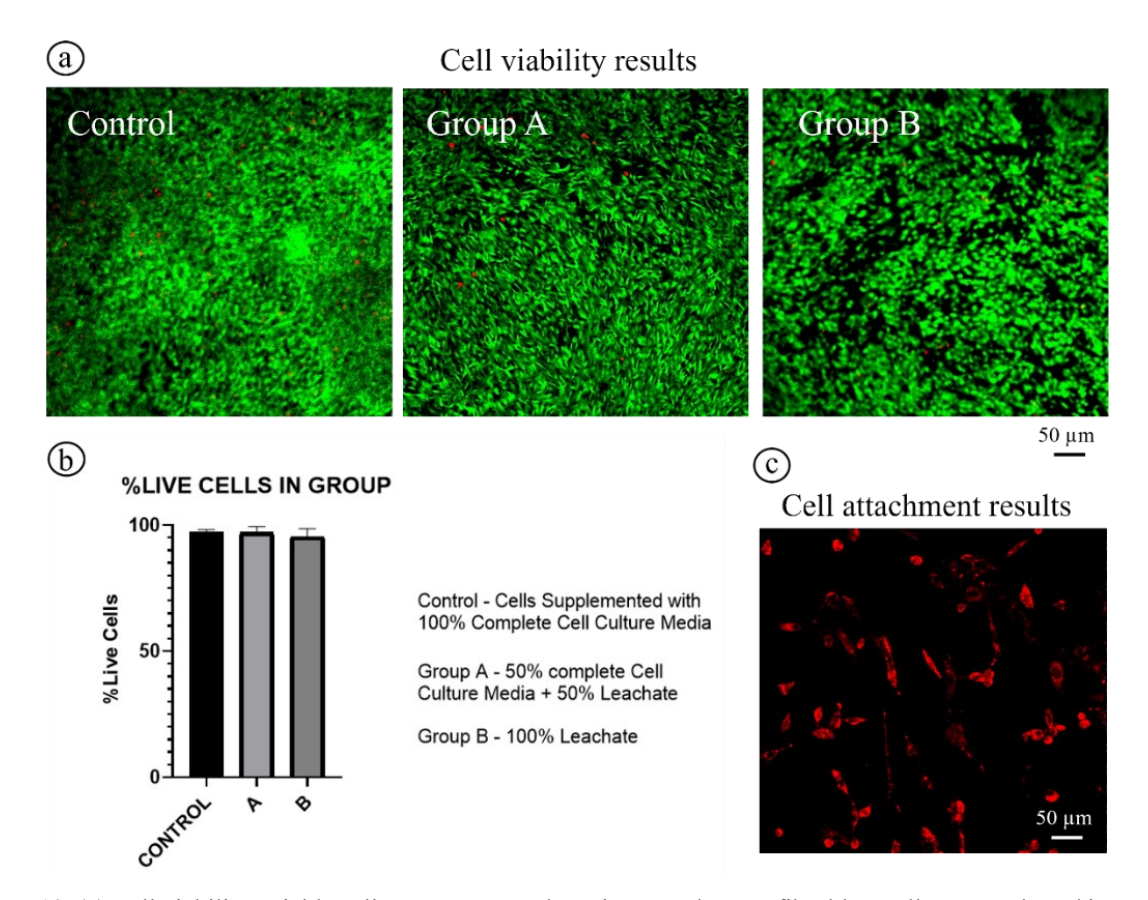


Figure 12. (a) Cell viability: Viable cells are present at day 5 in control group fibroblast cells were cultured in complete media, Group A fibroblast cells were exposed to a mixture of 1:1 ratio of CoCrMo-exposed leachate to complete media, and group B fibroblast cells were cultured in the leachate + 10% FBS. Live cells stain green and dead cells in red. Scale bars are 50  $\mu$ m. (b) 98-99% viability was observed in all groups (n=4). (c) cell attachment tests: fibroblast cells stained red with PKH26 Red Fluorescent Cell membrane marker are visualized on the CoCrMo sample surface. Cells have spread and adhered to the surface of the sample after 24 hours. Scale bars are 50  $\mu$ m (n=2).

# 4. Summary and Conclusion

In this investigation, the microstructural changes, mechanical performance, and cytotoxicity characteristics of binder jetted parts made from gas atomized Co-Cr-Mo powder were examined after sintering at various temperatures and optional aging. The findings can be summarized as follows:

- a. The initial density of the as-printed parts was approximately 50%. However, after undergoing a sintering process for 2 h at temperatures ranging from 1240 °C to 1380 °C, the relative densities significantly improved to 54% and 99.8%, respectively.
- b. Microscopy observations showed that the grain diameter of the sample sintered at 1240 °C was  $17.5 \pm 0.8$  µm, and increased to  $182.4 \pm 3.4$  µm after sintering at 1380 °C. The low-temperature regime showed slow densification with interconnected porosity and carbiderich phases. The intermediate sintering regime showed increased density, smaller pore networks, and a shift to an hcp matrix with nano-sized carbides at grain boundaries. The final sintering regime showed full densification, significant grain growth, and a clear, straight grain boundary. The highest temperature sintering regime likely involved supersolidus liquid phase sintering with complete pore filling, full densification, and

- significant grain growth. The study highlights the importance of temperature control and its effects on the microstructure of the sintered material.
- c. XRD was used to analyze phases in binder jetted Co-Cr-Mo alloy. As-received Co-Cr-Mo powder showed  $\gamma$ -Co single phase, while sintered Co matrix showed both  $\gamma$ -Co and  $\varepsilon$ -Co phases. A higher ratio of  $\gamma$ -Co to  $\varepsilon$ -Co phase transformation was observed at sintering temperatures of  $\geq 1360$  °C, with the fraction of hcp phase increasing to about 90% at 1360 °C and 95% at 1380 °C. After an aging treatment, diffraction peaks for Cr<sub>23</sub>C<sub>6</sub> and Cr-Mo phases were detected at the grain boundaries, but no oxide diffraction peaks were seen due to sintering under vacuum.
- d. The effect of sintering temperature and aging treatment on the mechanical properties of binder jet printed Co-Cr-Mo alloy was investigated. Microhardness increased with increasing sintering temperature, reaching 325 HV<sub>0.1</sub> at 1380 °C, and was further enhanced to 522 HV<sub>0.1</sub> after aging at 800 °C for 24 h due to carbide formation and phase transformation. Ultimate yield strength and ultimate tensile strength increased after aging, but ductility decreased. Fractography analysis showed mostly brittle fracture with minimal ductile features in the sintered specimens and partially transgranular fracture with wedge-type cracks in the aged specimens.
- e. Cell viability and attachment tests were performed on 3T3 fibroblast cells exposed to elemental leachate from a Co-Cr-Mo sample. The viability test showed an average of 97±1% live cells in the control group, and 95±2% in the experimental groups, indicating favorable conditions for cell growth and survival. The attachment test showed successful attachment of the cells to the samples, with an average area of cells attached of 8±2% after 24 h of contact. These results suggest that the elemental leachate did not significantly affect the viability and confluency of the cells, and that the cells were able to attach to the Co-Cr-Mo sample, indicating good biocompatibility.

# Acknowledgements

AM would like to acknowledge the startup funding from the Department of Mechanical, Materials and Aerospace Engineering and Armour College of Engineering at Illinois Institute of Technology at Chicago, Illinois. Also, partial support from the National Science Foundation under grant number DMR-2050916 as well as Educational and Research Initiative Fund (ERIF) at IIT are appreciated by MK, PS, MKV, and AM. Funding for this work was provided, in part, by the Pritzker Institute of Biomedical Science and Engineering RES-MATCH program (undergraduate research opportunity for PS). This research was also partially funded by the Commonwealth of Pennsylvania's Department of Community and Economic Development (DCED) and the PA Manufacturing Innovation Program (PAMIP), acknowledged by AM, PRDV, and MC. PRDV was partially funded by the Swanson School of Engineering and the Office of the Provost of the University of Pittsburgh. AM, PRDV, and MC also acknowledge the Nanoscale Fabrication and Characterization Facility (NFCF) at the University of Pittsburgh.

## References

- [1] A. Costello, J. Sears, Repair opportunities for aerospace components through laser powder deposition, 305 (2019). https://doi.org/10.2351/1.5060818.
- [2] Y. Xia, J. Zhao, Z. Dong, X. Guo, Q. Tian, Y. Liu, A Novel Method for Making Co-Cr-Mo

- Alloy Spherical Powder by Granulation and Sintering, Jom. 72 (2020) 1279–1285. https://doi.org/10.1007/s11837-020-04009-7.
- [3] T.J. Webster, J.U. Ejiofor, Increased osteoblast adhesion on nanophase metals:, 25 (2004) 4731–4739. https://doi.org/10.1016/j.biomaterials.2003.12.002.
- [4] A. Frenk, W. Kurz, Microstructural effects on the sliding wear resistance of a cobalt-based alloy, Wear. 174 (1994) 81–91.
- [5] C.D. Opris, R. Liu, M.X. Yao, X.J. Wu, Development of Stellite alloy composites with sintering/HIPing technique for wear-resistant applications, Mater. Des. 28 (2007) 581–591.
- [6] P. Huang, Ro. Liu, X. Wu, M.X. Yao, Effects of Molybdenum Content and Heat Treatment on Mechanical and Tribological Properties of a Low-Carbon Stellite ® Alloy, J. Eng. Mater. Technol. 129 (2007) 523–529. https://doi.org/10.1115/1.2744429.
- [7] R. Rosenthal, B.R. Cardoso, I.S. Bott, R.P.R. Paranhos, E.A. Carvalho, Phase characterization in as-cast F-75 Co Cr Mo C alloy, (2010) 4021–4028. https://doi.org/10.1007/s10853-010-4480-x.
- [8] G. Herranz, C. Berges, J.A. Naranjo, C. García, I. Garrido, Mechanical performance, corrosion and tribological evaluation of a Co–Cr–Mo alloy processed by MIM for biomedical applications, J. Mech. Behav. Biomed. Mater. 105 (2020) 103706. https://doi.org/10.1016/j.jmbbm.2020.103706.
- [9] M. Mori, K. Yamanaka, K. Kuramoto, K. Ohmura, T. Ashino, A. Chiba, Effect of carbon on the microstructure, mechanical properties and metal ion release of Ni-free Co Cr Mo alloys containing nitrogen, Mater. Sci. Eng. C. 55 (2015) 145–154. https://doi.org/10.1016/j.msec.2015.05.058.
- [10] ASTM F75: Standard Specification for Cobalt-28 Chromium-6 Molybdenum Alloy Castings and Casting Alloy for Surgical Implants (UNS R30075) 1, ASTM Int. (2019). https://doi.org/10.1520/F0075-18.2.
- [11] K. Yamanaka, M. Mori, A. Chiba, Enhanced Mechanical Properties of As-Forged Co-Cr-Mo-N Alloys with Ultrafine-Grained Structures, 43 (2012). https://doi.org/10.1007/s11661-012-1288-0.
- [12] Y. Okazaki, Effects of heat treatment and hot forging on microstructure and mechanical properties of Co-Cr-Mo alloy for surgical implants, Mater. Trans. 49 (2008) 817–823. https://doi.org/10.2320/matertrans.MRA2007274.
- [13] S. Hasan, A. Mazid, R.E. Clegg, The Basics of Stellites in Machining Perspective, 1 (2016) 35–50.
- [14] P. V Muterlle, M. Zendron, M. Perina, R. Bardini, A. Molinari, Microstructure and tensile properties of metal injection molding, (2010) 1091–1099. https://doi.org/10.1007/s10853-009-4051-1.
- [15] N. Koju, S. Niraula, B. Fotovvati, Additively Manufactured Porous Ti6Al4V for Bone Implants: A Review, Metals (Basel). 12 (2022).
- [16] A. Mostafaei, J. Gordon, A.D. Rollett, Additive Manufacturing of Cobalt Alloys, in: ASM Handb. Addit. Manuf. Process., 2020: p. Vol. 24.
- [17] P. Ganesh, A. Moitra, P. Tiwari, S. Sathyanarayanan, H. Kumar, S.K. Rai, R. Kaul, C.P. Paul, R.C. Prasad, L.M. Kukreja, Fracture behavior of laser-clad joint of Stellite 21 on AISI 316L stainless steel, Mater. Sci. Eng. A. 527 (2010) 3748–3756. https://doi.org/10.1016/j.msea.2010.03.017.
- [18] J.H. Rao, N. Stanford, On the Processing Feasibility, Microstructure Evolution, and Mechanical Properties of Laser Clad Stellite O 21 Alloy, J. Therm. Spray Technol. (2021).

- https://doi.org/10.1007/s11666-020-01129-z.
- [19] K.M. Mantrala, M. Das, V.K. Balla, C.S. Rao, V.V.S. Kesava Rao, Additive Manufacturing of Co-Cr-Mo Alloy: Influence of Heat Treatment on Microstructure, Tribological, and Electrochemical Properties, Front. Mech. Eng. 1 (2015) 1–7. https://doi.org/10.3389/fmech.2015.00002.
- [20] K.M. Mantrala, M. Das, V.K. Balla, C. Srinivasa Rao, V.V.S. Kesava Rao, Laser-deposited CoCrMo alloy: Microstructure, wear, and electrochemical properties, J. Mater. Res. 29 (2014) 2021–2027. https://doi.org/10.1557/jmr.2014.163.
- [21] F.A. España, V.K. Balla, S. Bose, A. Bandyopadhyay, Design and fabrication of CoCrMo alloy based novel structures for load bearing implants using laser engineered net shaping, Mater. Sci. Eng. C. 30 (2010) 50–57.
- [22] K. Monroy, J. Delgado, J. Ciurana, Study of the pore formation on CoCrMo alloys by selective laser melting manufacturing process, Procedia Eng. 63 (2013) 361–369. https://doi.org/10.1016/j.proeng.2013.08.227.
- [23] C. dos Santos, A.F. Habibe, B.G. Simba, J.F.C. Lins, B.X. de Freitas, C.A. Nunes, CoCrMobase alloys for dental applications obtained by selective laser melting (slm) and cad/cam milling, Mater. Res. 23 (2020) 1–6. https://doi.org/10.1590/1980-5373-MR-2019-0599.
- [24] Z. Guoqing, L. Junxin, Z. Xiaoyu, L. Jin, W. Anmin, Effect of Heat Treatment on the Properties of CoCrMo Alloy Manufactured by Selective Laser Melting, J. Mater. Eng. Perform. 27 (2018) 2281–2287. https://doi.org/10.1007/s11665-018-3351-5.
- [25] Y.S. Hedberg, B. Qian, Z. Shen, S. Virtanen, I. Odnevall Wallinder, In vitro biocompatibility of CoCrMo dental alloys fabricated by selective laser melting, Dent. Mater. 30 (2014) 525–534. https://doi.org/10.1016/j.dental.2014.02.008.
- [26] K. Grandfield, A. Palmquist, S. Goncalves, A. Taylor, M. Taylor, L. Emanuelsson, P. Thomsen, H. Engqvist, Free form fabricated features on CoCr implants with and without hydroxyapatite coating in vivo: a comparative study of bone contact and bone growth induction, (2011) 899–906. https://doi.org/10.1007/s10856-011-4253-3.
- [27] X. Yan, H. Lin, Y. Wu, W. Bai, Effect of two heat treatments on mechanical properties of selective-laser-melted Co-Cr metal-ceramic alloys for application in thin removable partial dentures, J. Prosthet. Dent. 119 (2018) 1028.e1-1028.e6.
- [28] Y. Kajima, A. Takaichi, N. Kittikundecha, T. Nakamoto, T. Kimura, N. Nomura, A. Kawasaki, T. Hanawa, H. Takahashi, N. Wakabayashi, Effect of heat-treatment temperature on microstructures and mechanical properties of Co–Cr–Mo alloys fabricated by selective laser melting, Mater. Sci. Eng. A. 726 (2018) 21–31.
- [29] G. Yingfei, P.M. de Escalona, A. Galloway, Influence of Cutting Parameters and Tool Wear on the Surface Integrity of Cobalt-Based Stellite 6 Alloy When Machined Under a Dry Cutting Environment, J. Mater. Eng. Perform. 26 (2017) 312–326.
- [30] Y. Lu, S. Wu, Y. Gan, S. Zhang, S. Guo, J. Lin, J. Lin, Microstructure, mechanical property and metal release of As-SLM CoCrW alloy under different solution treatment conditions, J. Mech. Behav. Biomed. Mater. 55 (2015) 179–190.
- [31] B. Ren, C. Chen, M. Zhang, Effect of heat treatment on the microstructure of Co-Cr-W alloy fabricated by laser additive manufacturing, Opt. Eng. 57 (2018).
- [32] K. Myers, P. Cortes, B. Conner, T. Wagner, B. Hetzel, K.M. Peters, Structure property relationship of metal matrix syntactic foams manufactured by a binder jet printing process, Addit. Manuf. 5 (2015) 54–59.
- [33] A. Mostafaei, E. Stevens, E. Hughes, S. Biery, C. Hilla, M. Chmielus, Powder bed binder

- jet printed alloy 625: densification, microstructure and mechanical properties, Mater. Des. 108 (2016) 126–135.
- [34] A. Mostafaei, P. Rodriguez De Vecchis, E.L.E.L. Stevens, M. Chmielus, Sintering regimes and resulting microstructure and properties of binder jet 3D printed Ni-Mn-Ga magnetic shape memory alloys, Acta Mater. 154 (2018) 355–364. https://doi.org/https://doi.org/10.1016/j.actamat.2018.05.047.
- [35] A. Mostafaei, K.A. Kimes, E.L. Stevens, J. Toman, Y.L. Krimer, K. Ullakko, M. Chmielus, Microstructural evolution and magnetic properties of binder jet additive manufactured Ni-Mn-Ga magnetic shape memory alloy foam, Acta Mater. 131 (2017) 482–490.
- [36] A. Mostafaei, J. Toman, E.L. Stevens, E.T. Hughes, Y.L. Krimer, M. Chmielus, Microstructural evolution and mechanical properties of differently heat-treated binder jet printed samples from gas- and water-atomized alloy 625 powders, Acta Mater. 124 (2017) 280–289.
- [37] A. Mostafaei, E.L. Stevens, J.J. Ference, D.E. Schmidt, M. Chmielus, Binder jetting of a complex-shaped metal partial denture framework, Addit. Manuf. 21 (2018) 63–68.
- [38] A. Levy, A. Miriyev, A. Elliott, S.S. Babu, N. Frage, Additive manufacturing of complex-shaped graded TiC/steel composites, Mater. Des. (2017). https://doi.org/10.1016/j.matdes.2017.01.024.
- [39] D.-T. Chou, D. Wells, D. Hong, B. Lee, H. Kuhn, P.N. Kumta, Novel processing of iron—manganese alloy-based biomaterials by inkjet 3-D printing, Acta Biomater. 9 (2013) 8593—8603.
- [40] D. Hong, D.-T.T. Chou, O.I. Velikokhatnyi, A. Roy, B. Lee, I. Swink, I. Issaev, H.A. Kuhn, P.N. Kumta, Binder-jetting 3D printing and alloy development of new biodegradable Fe-Mn-Ca/Mg alloys, Acta Biomater. 45 (2016) 1–12. http://linkinghub.elsevier.com/retrieve/pii/S1742706116304287.
- [41] A. Butscher, M. Bohner, N. Doebelin, L. Galea, O. Loeffel, R. Müller, Moisture based three-dimensional printing of calcium phosphate structures for scaffold engineering, Acta Biomater. 9 (2013) 5369–5378. https://doi.org/10.1016/j.actbio.2012.10.009.
- [42] A. Zocca, P. Colombo, C.M. Gomes, J. Günster, Additive Manufacturing of Ceramics: Issues, Potentialities, and Opportunities, J. Am. Ceram. Soc. 98 (2015) 1983–2001.
- [43] W.S.W. Harun, M.S.I.N. Kamariah, N. Muhamad, S.A.C. Ghani, F. Ahmad, Z. Mohamed, A review of powder additive manufacturing processes for metallic biomaterials, Powder Technol. 327 (2018) 128–151.
- [44] A. Basalah, Y. Shanjani, S. Esmaeili, E. Toyserkani, Characterizations of additive manufactured porous titanium implants, J. Biomed. Mater. Res. Part B Appl. Biomater. 100 B (2012) 1970–1979.
- [45] J.K. Sherwood, S.L. Riley, R. Palazzolo, S.C. Brown, C. Monkhouse, M. Coates, L.G. Griffith, L.K. Landeen, A. Ratcliffe, A three-dimensional osteochondral composite scaffold for articular cartilage repair, Biomaterials. 23 (2002) 4739–4751.
- [46] M.N. Islam, S. Sacks, An experimental investigation into the dimensional error of powder-binder three-dimensional printing, Int. J. Adv. Manuf. Technol. 82 (2016) 1371–1380.
- [47] A. Mostafaei, A.M. Elliott, J.E. Barnes, C.L. Cramer, P. Nandwana, M. Chmielus, Binder jet 3D printing process parameters, materials, properties, modeling, and challenges, Prog. Mater. Sci. 119 (2021) 100707. https://doi.org/10.1016/j.pmatsci.2020.100707.
- [48] A.M. Elliott, C.L. Cramer, P. Nandwana, M. Chmielus, A. Mostafaei, Binder Jet-Metals, Encycl. Mater. Met. Alloy. 3 (2022) 120–133.

- [49] P. Stoyanov, K. Andre, P. Prichard, M. Yao, C. Gey, Microstructural and Mechanical Characterization of Mo-containing Stellite Alloys Produced by three Dimensional Printing, Procedia CIRP. 45 (2016) 167–170.
- [50] A. Mostafaei, P. Rodriguez De Vecchis, M.J.M.J. Buckenmeyer, S.R.S.R. Wasule, B.N.B.N. Brown, M. Chmielus, Microstructural evolution and resulting properties of differently sintered and heat-treated binder-jet 3D-printed Stellite 6, Mater. Sci. Eng. C. 102 (2019) 276–288. https://doi.org/10.1016/j.msec.2019.04.011.
- [51] R. Onler, A.S. Koca, B. Kirim, E. Soylemez, Multi-objective optimization of binder jet additive manufacturing of Co-Cr-Mo using machine learning, Int. J. Adv. Manuf. Technol. 119 (2022) 1091–1108. https://doi.org/10.1007/s00170-021-08183-z.
- [52] S. Vangapally, K. Agarwal, A. Sheldon, S. Cai, Effect of Lattice Design and Process Parameters on Dimensional and Mechanical Properties of Binder Jet Additively Manufactured Stainless Steel 316 for Bone Scaffolds, Procedia Manuf. 10 (2017) 750–759.
- [53] A. Mostafaei, E.L. Stevens, J.J. Ference, D.E. Schmidt, M. Chmielus, Binder jet printing of partial denture metal framework from metal powder, in: Mater. Sci. Technol., 2017: pp. 289–291.
- [54] A. Mostafaei, Powder bed binder jet 3D printing of Alloy 625: Microstructural evolution, densification kinetics and mechanical properties (thesis), University of Pittsburgh, 2018.
- [55] C.A. Schneider, W.S. Rasband, K.W. Eliceiri, NIH Image to ImageJ: 25 years of image analysis, Nat. Methods. 9 (2012) 671–675.
- [56] ASM-Standard, Metallography and Microstructures of Nonferrous Alloys, ASM Handb. 9 (2004) 711–751. https://doi.org/10.1361/asmhba0003769.
- [57] G. Matula, A. Szatkowska, K. Matus, B. Tomiczek, M. Pawlyta, Structure and Properties of Co-Cr-Mo Alloy Manufactured by Powder Injection Molding Method Grzegorz, Adv. Powder Metall. Part. Mater. 5 (1993). https://doi.org/10.3139/9781569908853.015.
- [58] M. Atapour, S. Sanaei, Z. Wei, M. Sheikholeslam, J.D. Henderson, U. Eduok, Y.K. Hosein, D.W. Holdsworth, Y.S. Hedberg, H.R. Ghorbani, In vitro corrosion and biocompatibility behavior of CoCrMo alloy manufactured by laser powder bed fusion parallel and perpendicular to the build direction, Electrochim. Acta. 445 (2023) 142059. https://doi.org/10.1016/j.electacta.2023.142059.
- [59] A. Kummrow, M. Frankowski, N. Bock, C. Werner, T. Dziekan, J. Neukammer, Quantitative assessment of cell viability based on flow cytometry and microscopy, Cytom. Part A. 83 A (2013) 197–204. https://doi.org/10.1002/cyto.a.22213.
- [60] P. Zhu, J. Chen, P. Li, S. Xu, Limitation of water-soluble tetrazolium salt for the cytocompatibility evaluation of zinc-based metals, Materials (Basel). 14 (2021) 4–13. https://doi.org/10.3390/ma14216247.
- [61] S.P. Pilipchuk, M.K. Vaicik, J.C. Larson, E. Gazyakan, M.H. Cheng, E.M. Brey, Influence of crosslinking on the stiffness and degradation of dermis-derived hydrogels, J. Biomed. Mater. Res. Part A. 101 (2013) 2883–2895. https://doi.org/10.1002/jbm.a.34602.
- [62] U. Malayoglu, A. Neville, Comparing the performance of HIPed and Cast Stellite 6 alloy in liquid-solid slurries, Wear. 255 (2003) 181–194.
- [63] D. de Castro Girão, M. Béreš, A.L. Jardini, R.M. Filho, C.C. Silva, A. de Siervo, H.F. Gomes de Abreu, W.S. Araújo, An assessment of biomedical CoCrMo alloy fabricated by direct metal laser sintering technique for implant applications, Mater. Sci. Eng. C. 107 (2020). https://doi.org/10.1016/j.msec.2019.110305.
- [64] G. Barucca, E. Santecchia, G. Majni, E. Girardin, E. Bassoli, L. Denti, A. Gatto, L. Iuliano,

- T. Moskalewicz, P. Mengucci, Structural characterization of biomedical Co-Cr-Mo components produced by direct metal laser sintering, Mater. Sci. Eng. C. 48 (2015) 263–269. https://doi.org/10.1016/j.msec.2014.12.009.
- [65] A. Ziębowicz, K. Matus, M. Pawlyta, W. Pakieła, G. Matula, Comparison of the crystal structure and wear resistance of co-based alloys with low carbon content manufactured by selective laser sintering and powder injection molding, Crystals. 10 (2020). https://doi.org/10.3390/cryst10030197.
- [66] Z. Wang, S.Y. Tang, S. Scudino, Y.P. Ivanov, R.T. Qu, D. Wang, C. Yang, W.W. Zhang, A.L. Greer, J. Eckert, K.G. Prashanth, Additive manufacturing of a martensitic Co-Cr-Mo alloy: towards circumventing the strength–ductility trade-off, Opt. Int. J. Light Electron Opt. (2020) 163947. https://doi.org/10.1016/j.addma.2020.101725.
- [67] B. Xavier, D. Freitas, C. Angelo, Sintering behaviour of Co-28 % Cr-6 % Mo compacted blocks for dental prosthesis, Integr. Med. Res. 8 (2019) 2052–2062. https://doi.org/10.1016/j.jmrt.2018.12.020.
- [68] C. Song, H. Park, H. Seong, H.F. López, Development of athermal and isothermal ε-martensite in atomized Co-Cr-Mo-C implant alloy powders, Metall. Mater. Trans. A Phys. Metall. Mater. Sci. 37 (2006) 3197–3204. https://doi.org/10.1007/BF02586154.
- [69] J.W. Sears, C. Allen, A. Holliday, Binder-Jet 3D Direct Metal Printing of Cobalt Chrome Moly Alloy James W. Sears, Christopher Allen, and Andrew Holliday, Carpenter Technology Corporation, Reading, PA 19601, AMPM 2019 Conf. Phoenix, Arizona. (2019) 312–321.
- [70] M. Dourandish, D. Godlinski, A. Simchi, V. Firouzdor, Sintering of biocompatible P / M Co Cr Mo alloy (F-75) for fabrication of porosity-graded composite structures, 472 (2008) 338–346. https://doi.org/10.1016/j.msea.2007.03.043.
- [71] S. Zangeneh, E. Erisir, M. Abbasi, A. Ramazani, Evaluation of the aging effect on the microstructure of co-28cr-6mo-0.3c alloy: Experimental characterization and computational thermodynamics, Metals (Basel). 9 (2019) 1–14. https://doi.org/10.3390/met9050581.
- [72] P. Suri, R.P. Koseski, R.M. German, Microstructural evolution of injection molded gas- and water-atomized 316L stainless steel powder during sintering, 402 (2005) 341–348. https://doi.org/10.1016/j.msea.2005.01.004.
- [73] A.J.T. Clemow, B.L. Daniell, Solution treatment behavior of Co-Cr-Mo alloy, J. Biomed. Mater. Res. 13 (1979) 265–279. https://doi.org/10.1002/jbm.820130208.
- [74] E. Bettini, T. Eriksson, M. Boström, C. Leygraf, J. Pan, Influence of metal carbides on dissolution behavior of biomedical CoCrMo alloy: SEM, TEM and AFM studies, Electrochim. Acta. 56 (2011) 9413–9419. https://doi.org/10.1016/j.electacta.2011.08.028.
- [75] R.M. German, Coarsening in sintering: Grain shape distribution, grain size distribution, and grain growth kinetics in solid-pore systems, Crit. Rev. Solid State Mater. Sci. 35 (2010) 263–305.
- [76] A. Salinas-rodriguez, H.F. Lopez, FCC to HCP transformation kinetics in a Co 27Cr 5Mo 0 . 23C alloy, 9 (2010). https://doi.org/10.1007/s10853-010-4969-3.
- [77] H.F. López, A.J. Saldivar-Garcia, Martensitic transformation in a cast Co-Cr-Mo-C alloy, Metall. Mater. Trans. A Phys. Metall. Mater. Sci. 39 (2008) 8–18. https://doi.org/10.1007/s11661-007-9370-8.
- [78] M. Roudnicka, J. Bigas, O. Molnarova, D. Palousek, D. Vojtech, Different response of cast and 3d-printed co-cr-mo alloy to heat treatment: A thorough microstructure

- characterization, Metals (Basel). 11 (2021). https://doi.org/10.3390/met11050687.
- [79] I. Marek, P. Novák, J. Mlynár, D. Vojtěch, T.F. Kubatík, J. Málek, Powder metallurgy preparation of Co-based alloys for biomedical applications, Acta Phys. Pol. A. 128 (2015) 597–601.
- [80] W. Gui, H.Z.H. Long, T. Jin, X.S. Qi, Formation Mechanism of Lamellar M 23 C 6 Carbide in a Cobalt- Base Superalloy During Thermal Exposure at 1000 ° C, Acta Metall. Sin. (English Lett. (2017) 2–7. https://doi.org/10.1007/s40195-017-0596-1.
- [81] J.P. Moffat, T.E. Whitfield, K.A. Christofidou, E.J. Pickering, N.G. Jones, H.J. Stone, The Effect of Heat Treatment on the Oxidation Resistance of Cobalt-Based Superalloys James, (2020) 1–15.
- [82] Y. Liao, R. Pourzal, P. Stemmer, M.A. Wimmer, J.J. Jacobs, A. Fischer, L.D. Marks, New insights into hard phases of CoCrMo metal-on-metal hip replacements, J. Mech. Behav. Biomed. Mater. 12 (2012) 39–49.
- [83] T. Kilner, W.M. Laanemäe, R. Pilliar, G.C. Weatherly, S.R. MacEwen, Static mechanical properties of cast and sinter-annealed cobalt-chromium surgical implants, J. Mater. Sci. 21 (1986) 1349–1356. https://doi.org/10.1007/BF00553274.
- [84] M. Dourandish, D. Godlinski, A. Simchi, V. Firouzdor, Sintering of biocompatible P/M Co-Cr-Mo alloy (F-75) for fabrication of porosity-graded composite structures, Mater. Sci. Eng. A. 472 (2008) 338–346.
- [85] A. Mostafaei, P.R. De Vecchis, M.J. Buckenmeyer, S.R. Wasule, B.N. Brown, M. Chmielus, Microstructural evolution and resulting properties of differently sintered and heat-treated binder jet 3D printed Stellite 6, Mater. Sci. Eng. C. 102 (2019) 276–288.
- [86] P. Crook, Cobalt and Cobalt Alloys, in: ASM Handbook: Properties and Selection: Nonferrous Alloys and Special-Purpose Materials, 1990.
- [87] ASTM F75-23, Standard Specification for Cobalt-28 Chromium-6 Molybdenum Alloy Castings and Casting Alloy for Surgical Implants (UNS R30075), 2023.
- [88] M.F.F.A. Hamidi, W.S.W. Harun, M. Samykano, S.A.C. Ghani, Z. Ghazalli, F. Ahmad, A.B. Sulong, A review of biocompatible metal injection moulding process parameters for biomedical applications, Mater. Sci. Eng. C. 78 (2017) 1263–1276. https://doi.org/10.1016/j.msec.2017.05.016.
- [89] Z. Wang, S.Y. Tang, S. Scudino, Y.P. Ivanov, R.T. Qu, D. Wang, C. Yang, W.W. Zhang, A.L. Greer, J. Eckert, K.G. Prashanth, Additive manufacturing of a martensitic Co–Cr–Mo alloy: Towards circumventing the strength–ductility trade-off, Addit. Manuf. 37 (2021) 1–14. https://doi.org/10.1016/j.addma.2020.101725.
- [90] P. Mengucci, G. Barucca, A. Gatto, E. Bassoli, L. Denti, F. Fiori, E. Girardin, P. Bastianoni, B. Rutkowski, A. Czyrska-Filemonowicz, Effects of thermal treatments on microstructure and mechanical properties of a Co-Cr-Mo-W biomedical alloy produced by laser sintering, J. Mech. Behav. Biomed. Mater. 60 (2016) 106–117. https://doi.org/10.1016/j.jmbbm.2015.12.045.
- [91] K. Yamanaka, M. Mori, A. Chiba, Developing high strength and ductility in biomedical Co-Cr cast alloys by simultaneous doping with nitrogen and carbon, Acta Biomater. 31 (2016) 435–447. https://doi.org/10.1016/j.actbio.2015.12.011.
- [92] A. Mostafaei, S.H.V.R. Neelapu, C. Kisailus, L.M. Nath, T.D.B.B. Jacobs, M. Chmielus, Characterizing surface finish and fatigue behavior in binder-jet 3D-printed nickel-based superalloy 625, Addit. Manuf. 24 (2018) 200–209. https://doi.org/10.1016/j.addma.2018.09.012.